Supplemental Information

Non-quantum nanostructures-enabled hot carriers generation for enhancive photoelectrocatalytic oxidation of bio-alcohol in water coupled with hydrogen evolution

Pei-dong Wu [a], Lanyun Li [b], Keping Wang [b], Hu Li *[a,b], Zhen Fang *[b]

[a] Biomass Group, College of Engineering, Nanjing Agricultural University, 40 Dianjiangtai Road, Nanjing, Jiangsu 210031, China.

[b] National Key Laboratory of Green Pesticide, Key Laboratory of Green Pesticide and Agricultural Bioengineering, Ministry of Education, State-Local Joint Laboratory for Comprehensive Utilization of Biomass, Center for R&D of Fine Chemicals, Guizhou University, Guiyang, 550025, China.

* Corresponding authors.

E-mail: hli13@gzu.edu.cn (HL); zhenfang@njau.edu.cn (ZF)

1. Experimental section

Photoelectrode Characterization: The surface morphology and microstructure of the electrodes were characterized by ZEISS Sigma 500 field emission scanning electron microscope (SEM) and Thermo Scientific Talos F200X transmission electron microscope (TEM). The phase composition and surface electronic states and bonding characteristics of electrodes were characterized by PanAlytical X-ray diffractometer (XRD) and Thermo Scientific ESCALAB 250Xi X-ray photoelectron spectroscopy (XPS). The absorbance properties of the photoelectrodes were measured by a PerkinElmer ultraviolet-visible spectrophotometer (UV-Vis). The Steady-state photoluminescence (PL) and time-resolved PL of the electrode materials were tested by HORIBA LabRAM HR Evolution, and the steady-state PL and time-resolved PL were tested at different temperatures under the conditions of 325 nm laser excitation. The photoelectrochemical characterization was carried out using an electrochemical workstation (CHI 760E) and simulated sunlight (PLS-FX300HU). The photoelectrochemical properties were tested with BA oxidation using a two-chamber, three-electrode system with a prepared photoelectrode as the working electrode, a Pt electrode as the counter electrode, and a Hg/HgO electrode as the reference electrode.

Computational methods: All the density generalized function theory (DFT) calculations were performed using the PBE formulation in the generalized gradient approximation (GGA) employing the Vienna Ab Initio Package (VASP) [1-3]. Projection-enhanced wave (PAW) potentials were used to describe the ion nuclei, and valence electrons were taken into account using a plane wave basis set with a kinetic energy cutoff of 450 eV [4-5]. A Gaussian smearing method and a width of 0.05 eV were used to allow for partial occupancy of the Kohn-Sham orbitals. The electron energy is considered self-consistent when the energy change is less than 10^{-4} eV. The optimization of geometry is considered convergent when the change in force is less than 0.05 eV/Å. Grimme's DFT-D3 method is used to describe the dispersive interactions [6]. The Brillouin zone integral uses the surface structure of a 2 × 2 × 1 monkhorst package K-point sampling. The final adsorption energy (E_{ads}) was

calculated as Eads= $E_{ad/sub}$-E_{ad}-E_{sub}, where $E_{ad/sub}$, E_{ad} and E_{sub} are the optimized adsorbate/substrate system, the adsorbate in the structure and the initial substrate, respectively.

2. Additional discussions, Tables, and Figures

Table S1. Summary of selective oxidation of BA via representative photocatalytic/electrocatalytic/thermocatalytic/photoelectrocatalytic systems

Entry	Catalysts	Reaction conditions	Conv. (%)	BAD Sel. (%)	BEN Sel. (%)	Ref.
1	Au-BiOCl-O_V	Photocatalytic, CH_3CN solutions, 0.1 MPa O_2, 300-W Xe lamp, 8h	75.6	> 99	-	[7]
2	TiO_2/Ti_3C_2	Photocatalytic, n-Hexane solutions, O_2 atmosphere, UV-vis light irradiation, 5h	97	98	-	[8]
3	POM-$ZnIn_2S_4$	Photocatalytic, water solutions, Ar atmosphere, visible light, 5h	96	98	-	[9]
4	ZnTi-LDHs	Photocatalytic, benzotrifluoride solutions, O_2 atmosphere, UV-vis irradiation , 4h	61	77	-	[10]
5	Bi_2MoO_6	Photocatalytic, benzotrifluoride solutions, 0.1 MPa O_2, 300 W Xe arc lamp, 4h	38.2	99	-	[11]
6	$Ni/PdH_{0.43}$	Thermocatalytic, O_2 2atm, 100 °C	95	92	-	[12]
7	OCNT-800	Thermocatalytic, CH_3CN: H_2O (1:1), 50 °C	92	53	-	[13]
8	Ru-NPs@NCNTs	Electrocatalytic, 1.0 M KOH solution, 1.38 V vs. RHE	96	100	-	[14]
9	CuO	Electrocatalytic, 1.0 M KOH solution, 1.38 V vs. RHE	99	96	-	[15]
10	N-Mo-Ni/NF	Electrocatalytic, 1.0 M KOH solution, 1.34 V vs. RHE	99	-	98	[16]
11	G@U-LDH@BVO	Photoelectrocatalytic, PBS solution, 300 W Xe lamp, 1.2 V vs. RHE, 6 h	22	99	-	[17]
12	Mo-BVO-TiCoNO-$CoFeO_{xy}$	Photoelectrocatalytic, 1M NaOH solution, PLS-FX300HU, 1.48 V vs. RHE, 10 h	98.7	-	> 99	This work

Table S2. Equivalent-circuit fitting parameters of photoanodes

System	Series resistance, R_s (Ω)	Resistance, R_t (Ω)	Frequency power	CPE, Yo (× 10^{-6} F)	*Chsq*(× 10^{-4})	Warburg
BVO	15.72	3370.00	0.80	57.80	3.78	-
Mo-BVO	10.83	951.70	0.57	48.26	95.0	-
Mo-BVO-TiCoNO	97.74	52.56	0.80	2148.00	8.08	-
Mo-BVO-TiCoNO-CoO_{xy}	8.39	10.87	0.80	739.80	2.69	-
Mo-BVO-TiCoNO-FeO_{xy}	12.37	12.13	0.80	6.52	1.13	0.01
Mo-BVO-TiCoNO-$CoFeO_{xy}$	10.57	30.05	0.80	597.20	1.32	8.84
Mo-BVO-TiCoNO-$CoFeO_{xy}$ [a]	23.45	336.5	0.80	568.50	0.54	0.05
$CoFeO_{xy}$	47.16	283.1	0.80	3.32	7.60	-
$CoFeO_{xy}$ [a]	42.82	321.1	0.77	3.31	4.05	-

[a] In dark condition.

Table S3. Charge carriers' lifetime of Mo-BVO, Mo-BVO-TiCoNO and Mo-BVO-TiCoNO-$CoFeO_{xy}$

System	A (%)			τ (ns)			τ_{ave} (ns)
	A_1	A_2	A_3	τ_1	τ_2	τ_3	
Mo-BVO	34.8	65.2	-	62.5	1012.6	-	982.3
Mo-BVO-TiCoNO	30.8	20.6	48.6	518.9	48.3	5787.7	5486.0
Mo-BVO-TiCoNO-$CoFeO_{xy}$	29.3	7.0	63.7	233.0	24.5	3414.0	3314.9

Table S4. Charge carriers' lifetime of Mo-BVO-TiCoNO-$CoFeO_{xy}$ in different temperature

Temperature (K)	A (%)			τ (ns)			τ_{ave} (ns)
	A_1	A_2	A_3	τ_1	τ_2	τ_3	
200	27.9	18.3	53.8	275.7	27.0	3801.7	3665.4
270	29.4	7.8	62.7	273.9	26.5	3754.5	3636.3
300	29.3	7.0	63.7	233.0	24.5	3414.0	3314.9
340	25.3	30.0	44.6	120.0	925.3	8470.4	7894.8
410	15.5	30.5	54.0	78.0	653.7	6973.4	6635.6

Table S5. ICP elemental contents of Mo-BVO, Mo-BVO-TiCoNO, Mo-BVO-TiCoNO-FeO_{xy}, Mo-BVO-TiCoNO-CoO_{xy} and Mo-BVO-TiCoNO-$CoFeO_{xy}$

Photoanode	Mo (at %)	Bi (at %)	V (at %)	Co (at %)	Fe (at %)	S (at %)
Mo-BVO	3.0	46.3	50.7	-	-	-
Mo-BVO-TiCoNO	2.1	33.9	36.1	22.1	-	5.8
Mo-BVO-TiCoNO-CoO_{xy}	2.0	35.0	35.4	27.5	-	-
Mo-BVO-TiCoNO-FeO_{xy}	2.0	32.2	36.2	21.4	8.2	-
Mo-BVO-TiCoNO-$CoFeO_{xy}$	1.9	32.3	34.7	27.1	4.0	-

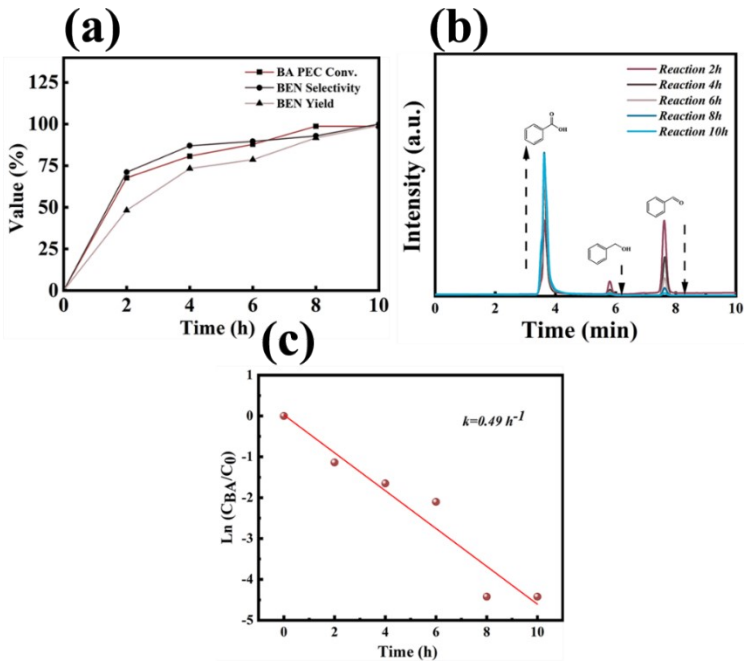

Figure S1. Different reaction times for converting benzyl alcohol (BA) to benzoic acid (BEN) (a), HPLC chromatogram traces of the various products (b) and Pseudo-first-order kinetic models of the BA oxidation (c) of Mo-BVO-TiCoNO-$CoFeO_{xy}$

Additional discussions: The HPLC chromatogram of the reaction mixture obtained from PEC oxidation of BA catalyzed by Mo-BVO-TiCoNO-$CoFeO_{xy}$ is shown in Figure S1b. The peak intensity of BEN can be found to increase gradually with reaction time, and the peak intensity of BA decreases, while the peak intensity of BAD first increases from zero and then decreases slowly. The BAD is present in the product distribution, however, the content of BAD is in a trace amount.

The oxidation process kinetic was determined by the following formula (1):

$$at + b = Ln\left(\frac{C_{BA}}{C_0}\right)\#(1)$$

where C_{BA} is the concentration of BA at reaction time t, C_0 is the starting concentration of BA, and a is the minus constant ($-k$ h^{-1}) determined by linear regression of ln C_{BA}/C_0 and t. The change of BA concentration as a function of time can be fitted to a pseudo-first-order kinetic model, and the kinetic constant (k) is 0.49 h^{-1}.

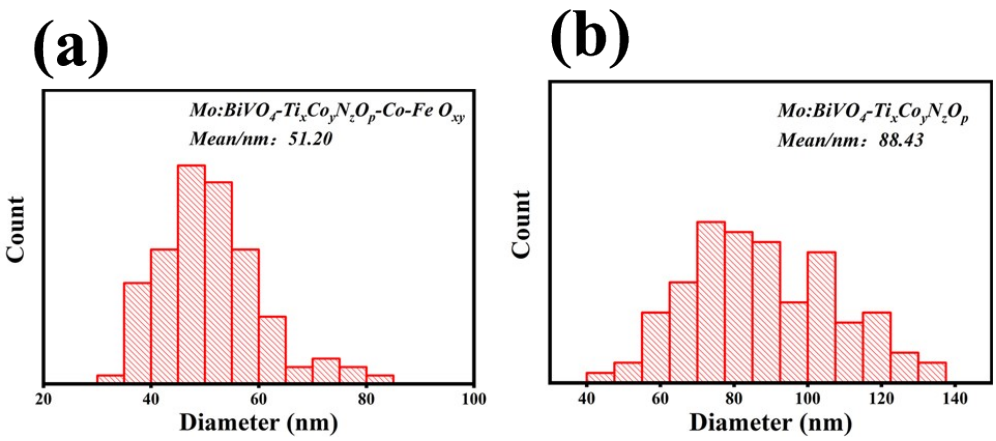

Figure S2. Non-quantum nanowires diameter distribution (SEM): Mo-BVO-TiCoNO-$CoFeO_{xy}$ (a) and Mo-BVO-TiCoNO (b)

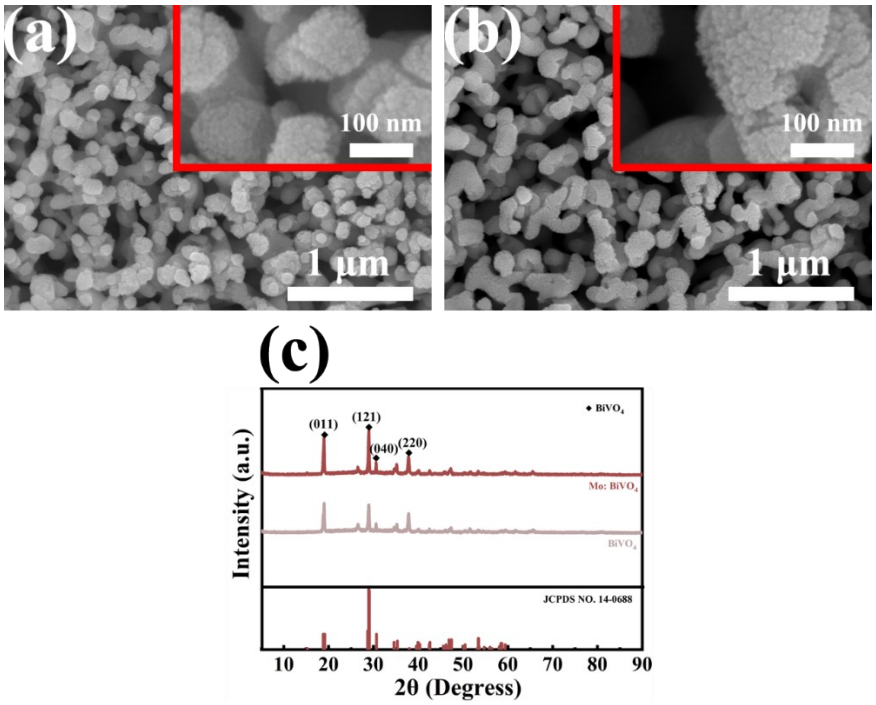

Figure S3. SEM images (a, b) and XRD spectra (c) of BVO and Mo-BVO

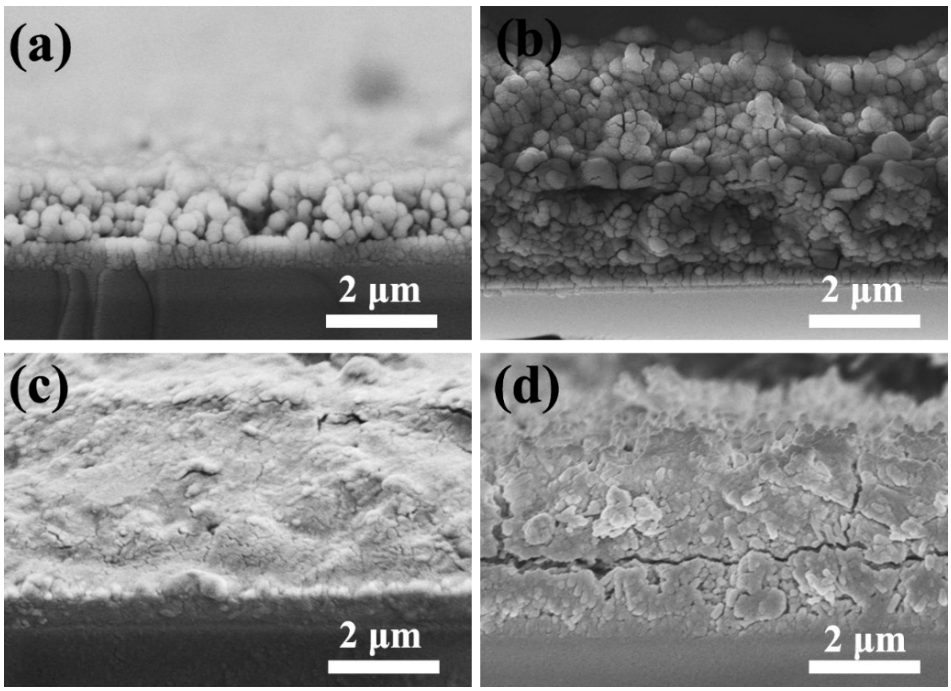

Figure S4. SEM side view images of Mo-BVO (a), Mo-BVO-TiCoNO (b), Mo-BVO-TiCoNO-FeO_{xy} (c) and Mo-BVO-TiCoNO-CoO_{xy} (d)

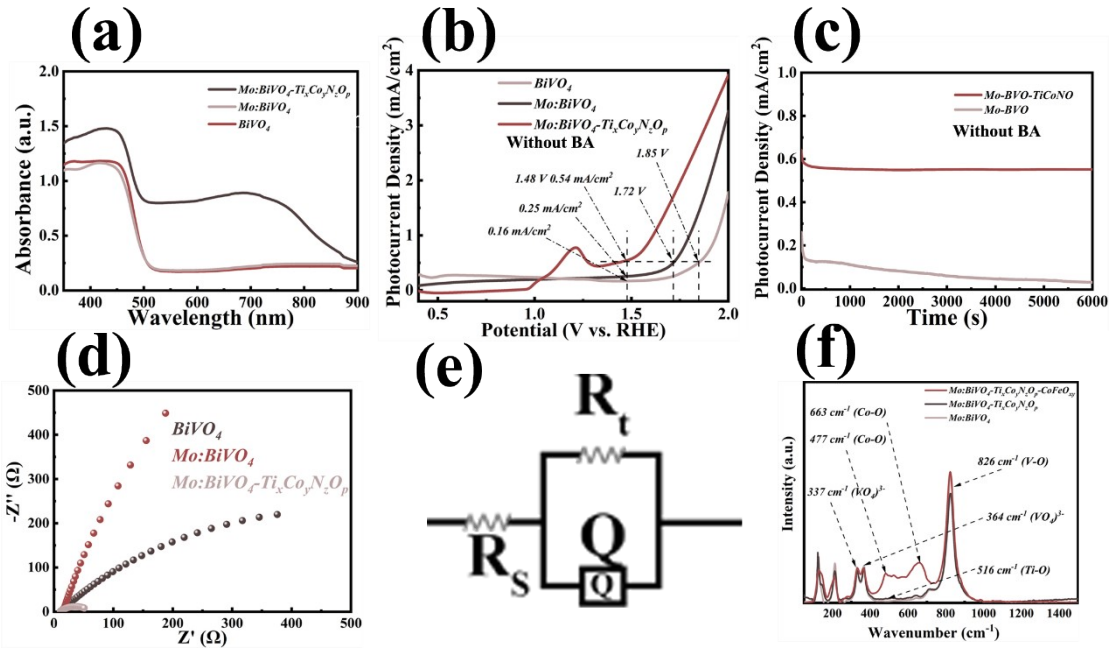

Figure S5. UV-Vis absorbance spectra (a), Current density-voltage curves (b), Time-current (I-t) curves (c), Electrochemical impedance spectroscopy (d), Fitting circuit (e) and Raman spectra (f) of BVO, Mo-BVO and Mo-BVO-TiCoNO

Additional discussions: Mo-BVO, as a semiconductor material with photoresponse, provides the basic photocurrent for the photoelectrode. The stability of Mo-BVO in alkaline environment is relatively weak, though, which requires the loading of TiCoNO protective layer to keep the photovoltaic electrode stable in this system for a long time. As shown in Figure S5c, the photocurrent of Mo-BVO photoelectrode decays rapidly in this system, while the photocurrent remains stable after loading the TiCoNO layer. The TiCoNO layer acts as a protective layer for the Mo-BVO substrate, otherwise, the photocurrent of Mo-BVO will be decayed rapidly under the strong alkaline system due to the precipitation of V^{5+} ions. Therefore, we introduced the TiCoNO layer to protect the Mo-BVO substrate. The Mo-BVO-TiCoNO photoelectrode for the yield of BA to BEN was found to be low (55.9%, Table 1), and therefore a metal oxide layer ($CoFeO_{xy}$) was considered to be loaded on it to improve the yield of the photoelectrode for BEN, reaching 97.7%. Raman characterization of Mo-BVO, Mo-BVO-TiCoNO, and Mo-BVO-TiCoNO-$CoFeO_{xy}$ has been tested. As shown in Figure S5f, all photoelectrodes were found to have unique characteristic

peaks, in which the characteristic peak at 826 cm^{-1} can be attributed to the strong symmetric stretching of V-O in Mo-BVO substrate. The characteristic peaks at 364 cm-1 and 337 cm^{-1} are ascribed to the symmetric and asymmetric modes of the V-O bond in the VO_4 structure, respectively, while the wavenumber of 216 cm^{-1} and 124 cm^{-1} are attributed to the external modes. The Raman band observed at 516 cm^{-1} after loading the TiCoNO layer is caused by the existence of the Ti-O bond. The characteristic peaks at 477 cm^{-1} and 663 cm^{-1} are observed for Mo-BVO-TiCoNO-$CoFeO_{xy}$ but absent for Mo-BVO and Mo-BVO-TiCoNO, which are resulted from the bending mode of the Co-O bond. The above analyses show that the loaded TiCoNO and CoFeOxy layers form a strict connection with the Mo-BVO of the substrate.

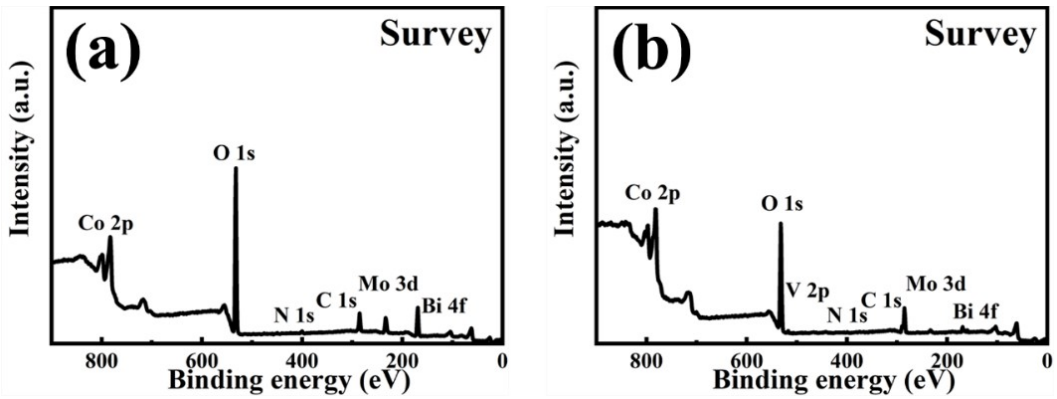

Figure S6. XPS survey spectra of Mo-BVO-TiCoNO (a) and Mo-BVO-TiCoNO-$CoFeO_{xy}$ (b)

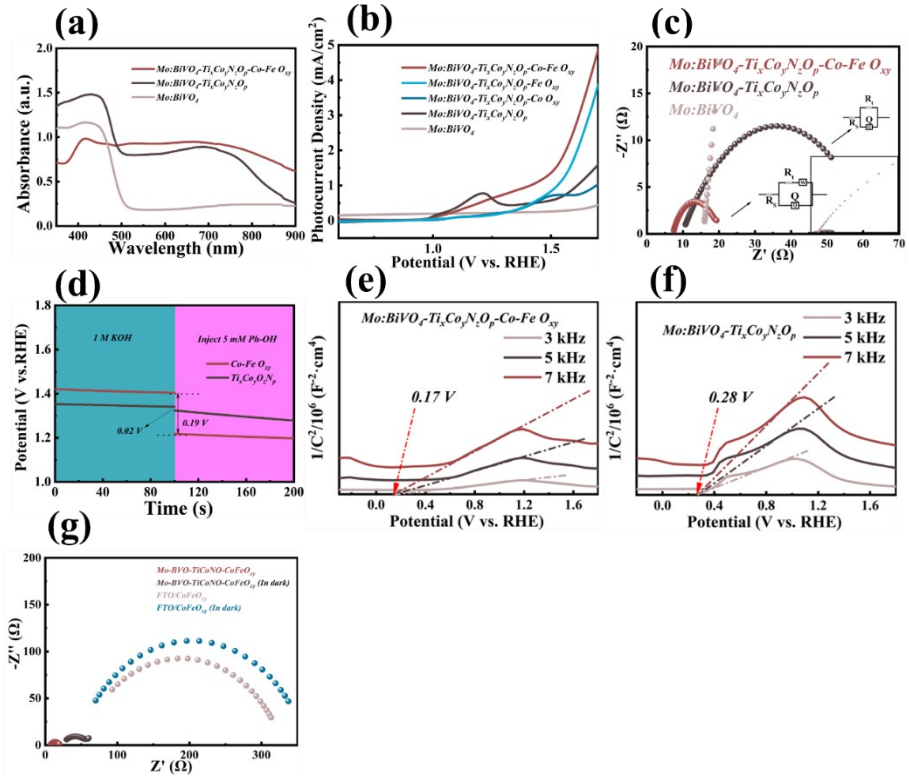

Figure S7. UV-Vis absorbance spectra (a), Current density-voltage curves (b), Electrochemical impedance spectroscopy (c), Open-circuit potential (d), Mott-Schottky curve (e-f), and Electrochemical impedance spectroscopy (in light or in dark) (g) of Mo-BVO-TiCoNO-CoFeO$_{xy}$ and FTO/CoFeO$_{xy}$

Additional discussions: The electrochemical impedance under dark conditions was performed to show an impedance of 336 ohms for Mo-BVO-TiCoNO-CoFeO$_{xy}$ (Figure S7g, Table S2). FTO/CoFeO$_{xy}$ was prepared for the purpose of clarification. The impedance of FTO/CoFeO$_{xy}$ was 321 ohms under dark conditions and 283 ohms under light conditions, which indicates that the CoFe species are in direct contact with the conducting substrate. However, the electrochemical impedance under light conditions is only 30 ohms, which indicates that under light conditions, the substrate Mo-BVO generates a large number of photoexcited carriers, resulting in a significant decrease in the electrochemical impedance of Mo-BVO-TiCoNO-CoFeO$_{xy}$. Therefore, light is an indispensable condition, which has a decisive effect on the reaction in the whole photoelectrochemical oxidation process.

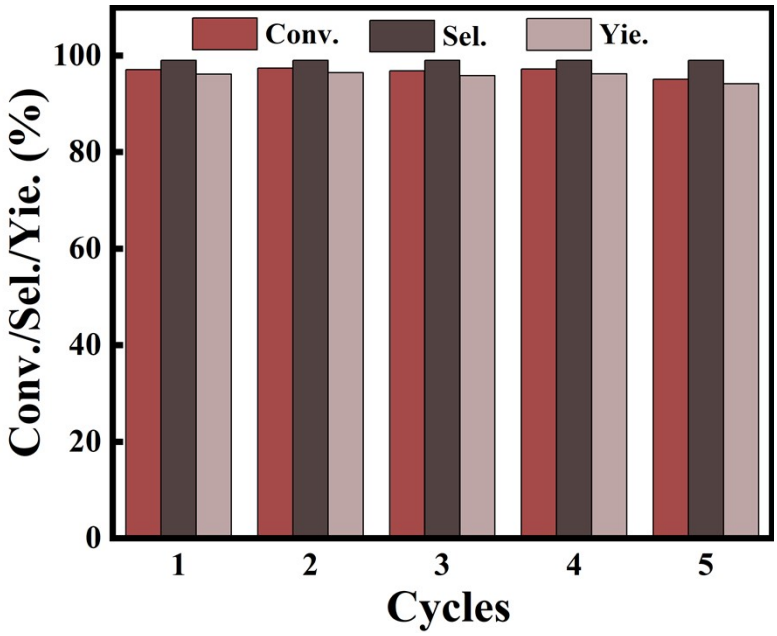

Figure S8. The activity of PEC BA oxidation with Mo-BVO-TiCoNO-$CoFeO_{xy}$ for 5 cycles

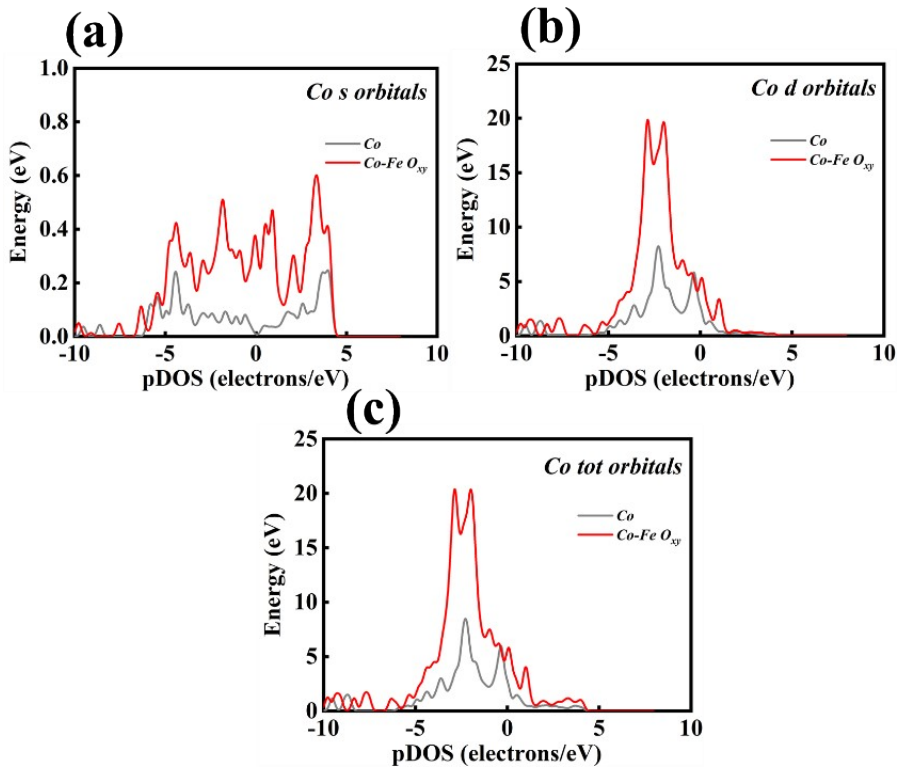

Figure S9. The Co s-orbitals (a), d-orbitals (b), and tot-orbitals (c) density of states of Mo-BVO-TiCoNO and Mo-BVO-TiCoNO-CoFeO$_{xy}$

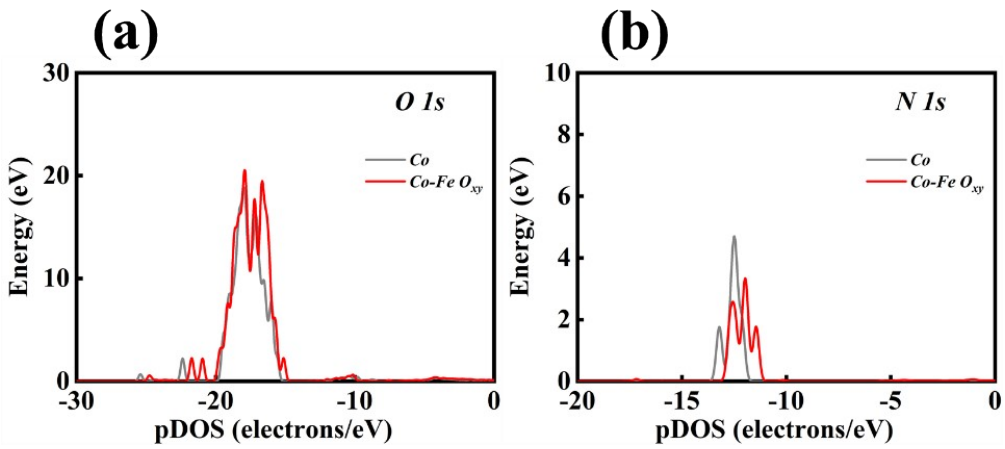

Figure S10. The O 1s orbitals (a) and N 1s orbitals (b) density of states of Mo-BVO-TiCoNO and Mo-BVO-TiCoNO-$CoFeO_{xy}$

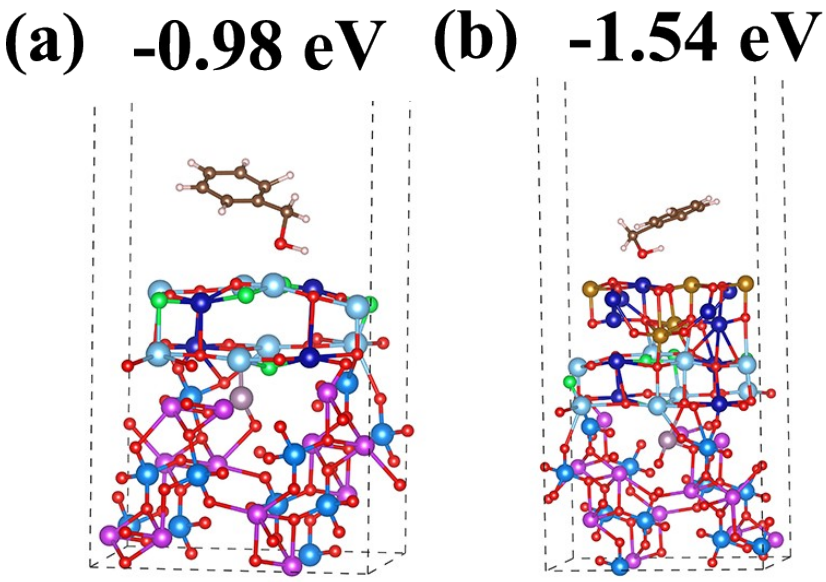

Figure S11. Benzyl alcohol adsorption energy of Mo-BVO-TiCoNO (a) and Mo-BVO-TiCoNO-$CoFeO_{xy}$ (b)

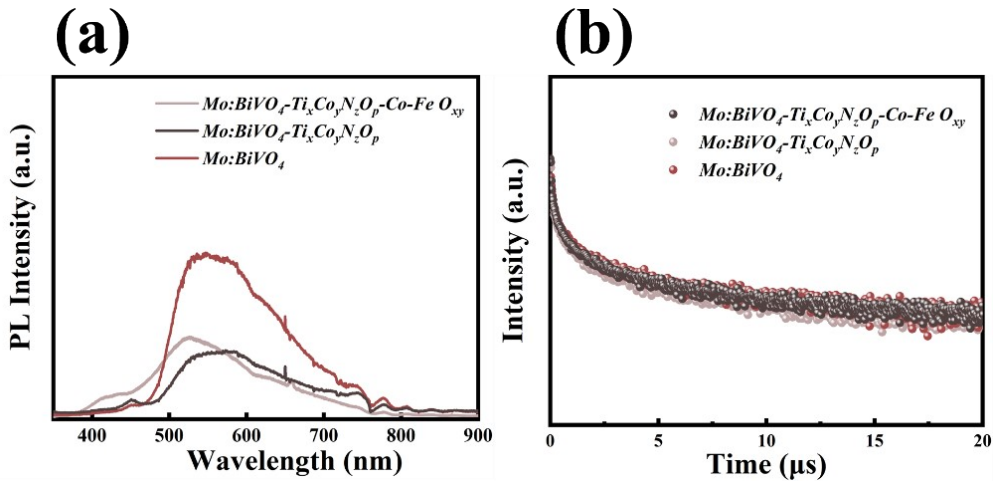

Figure S12. Steady-state photoluminescence (a) and time-resolved photoluminescence (b) of Mo-BVO, Mo-BVO-TiCoNO and Mo-BVO-TiCoNO-$CoFeO_{xy}$

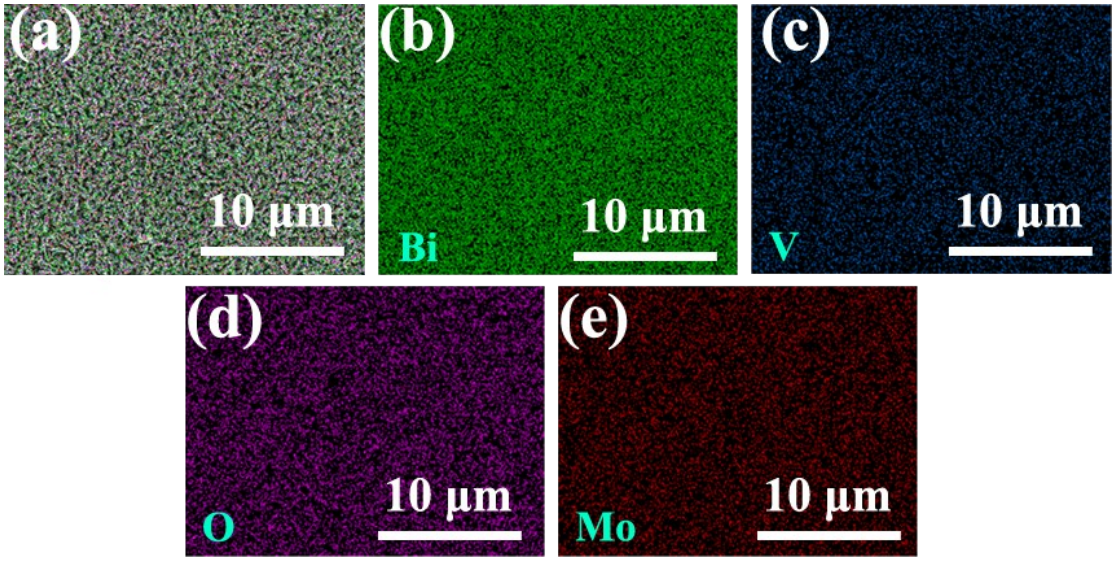

Figure S13. Element distribution mappings of Mo-BVO

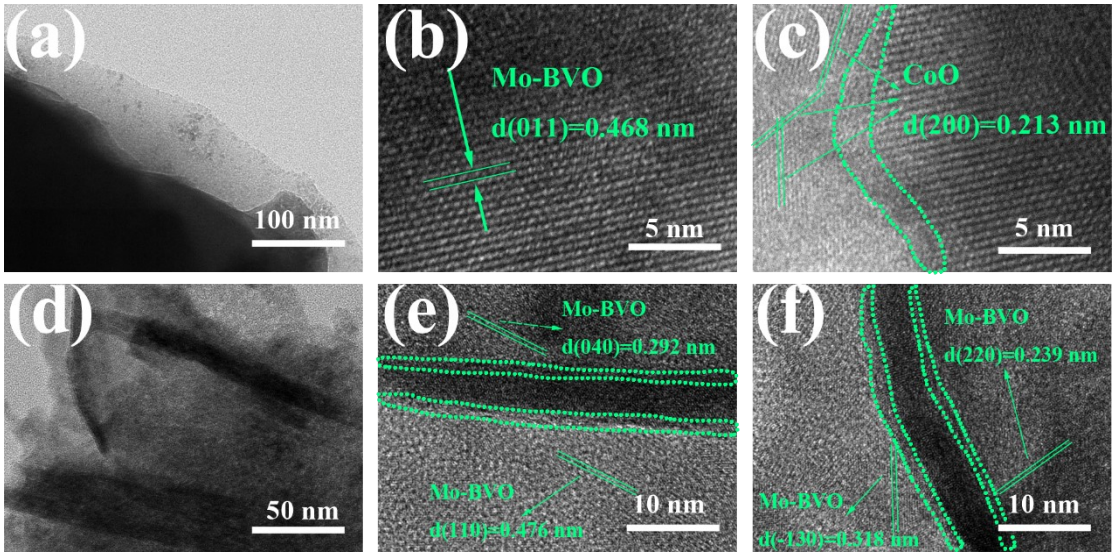

Figure S14. TEM images of Mo-BVO-TiCoNO (a-c) and Mo-BVO-TiCoNO-$CoFeO_{xy}$ (d-f)

Additional discussions: TEM characterization was used to investigate the distinctive micromorphology of $CoFeO_{xy}$ loading photoelectrode even further. Figure S14a-S14c shows the TEM of Mo-BVO-TiCoNO, the existence of a ~1.3 nm lattice dislocation layer between the Mo-BVO substrate and TiCoNO layer, the dislocation layer will make the photoexcited holes from the substrate layer more convenient to be transported to the surface layer to be involved in the BA oxidation reaction. As shown in Figure S14, lattice spacings of 0.239 nm, 0.292 nm, 0.318 nm, 0.468 nm, and 0.476 nm correspond to the (220), (040), (-130), (011), and (110) crystal planes of BVO, respectively. The (200) crystal plane of cobalt oxide corresponds to a lattice spacing of 0.213 nm. Figures S14d-S14f show the TEM of Mo-BVO-TiCoNO-$CoFeO_{xy}$, in which the edges of the non-quantum nanowire structure can be seen interacting with the electrode substrate material with well-defined interfacial interactions, a structure that leads to an increase in photoexcited carrier transport efficiency, in agreement with the DFT calculations.

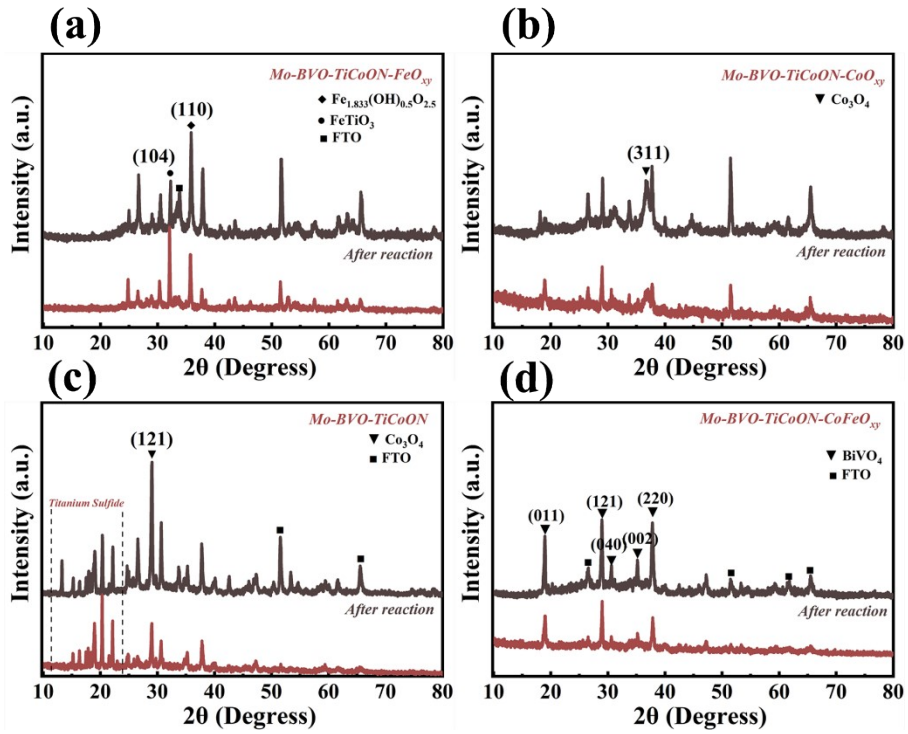

Figure S15. XRD spectra of used photoelectrodes Mo-BVO-TiCoNO-FeO$_{xy}$ (a), Mo-BVO-TiCoNO-CoO$_{xy}$ (b), Mo-BVO-TiCoNO (c) and Mo-BVO-TiCoNO-CoFeO$_{xy}$ (d)

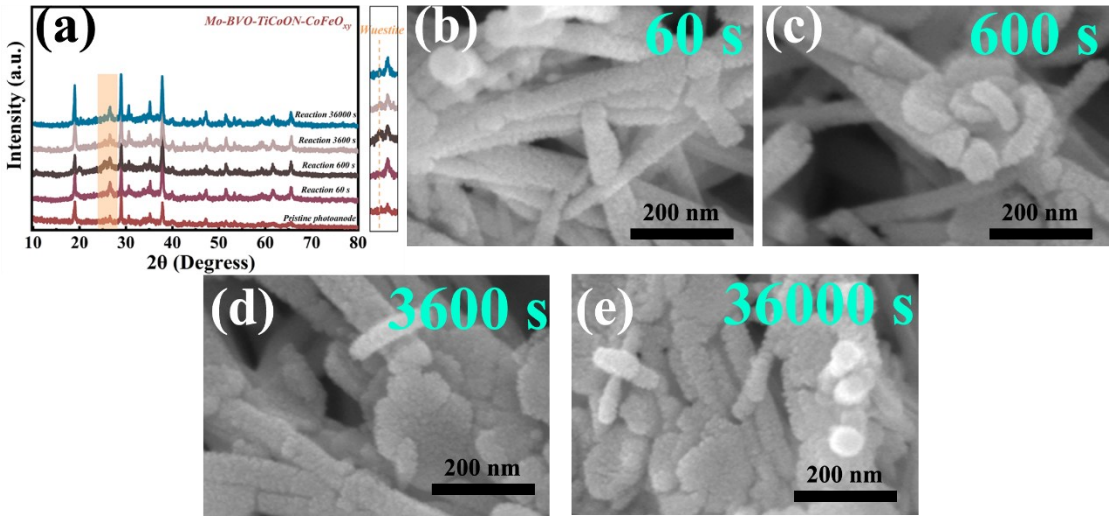

Figure S16. XRD spectra (a) and SEM images (b-e) of Mo-BVO-TiCoNO-FeO_{xy} after different reaction times

Additional discussions: Quasi in situ XRD (Figure S16a) of Mo-BVO-TiCoNO-$CoFeO_{xy}$ has been tested, which reveals a change in intensity of Fe species characteristic peaks with reaction time at 2θ of 26°. With the increase in the intensity of Fe species characteristic peak (until 600 s) the photocurrent is decreasing, as the reaction proceeds the intensity of Fe species characteristic peak decreases, while due to the hot carrier effect, the photocurrent is slowly increasing. The SEM of different reaction times is displayed in Figure S16b-e, revealing the appearance of flakes on the surface of the nanowires as the reaction time increases.

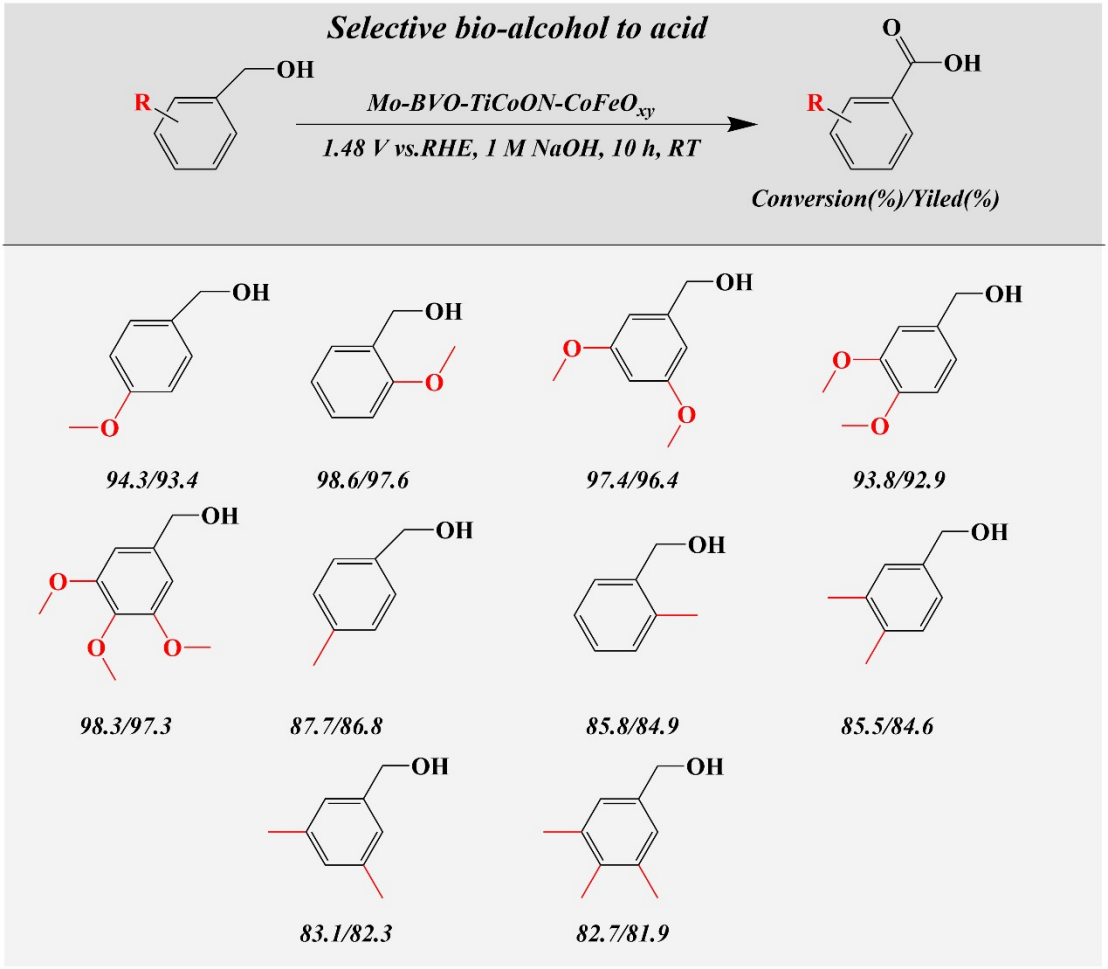

Figure S17. Substrate scope investigation

References

[1] G. Kresse and J. Furthmüller, *Phys. Rev. B.*, 1996, **54**, 11169.

[2] J. P. Perdew, K. Burke and M. Ernzerhof, *Phys. Rev. Lett.*, 1996, **77**, 3865.

[3] G Kresse and D Joubert, *Phys. Rev. B.*, 1999, **59**, 1758.

[4] P E Blöchl, *Phys. Rev. B.*, 1994, **50**, 17953.

[5] S Grimme, J Antony, S Ehrlich and H Krieg, *J. Chem. Phys.*, 2010, **132**, 154104.

[6] G Henkelman, B P. Uberuaga and H Jónsson, *J. Chem. Phys.*, 2000, **113**, 9901-9904.

[7] H Li, F Qin, Z Yang, X Cui, J Wang and L Zhang, *J. Am. Chem. Soc.*, 2017, **139**, 3513-3521.

[8] X Bao, H Li, Z Wang, F Tong, M Liu, Z Zheng, P Wang, H Cheng, Y Liu, Y Dai, Y Fan, Z Lie and B Huang, *Appl. Catal. B-Environ.*, 2021, **286**, 119885.

[9] F Xing, R Zeng, C Cheng, Q Liu, C Huang, *Appl. Catal. B-Environ.*, 2022, **306**, 121087.

[10] J Zou, Z Wang, W Guo, B Guo, Y Yu and L Wu, *Appl. Catal. B-Environ.*, 2020, **260**, 118185.

[11] K Jing, W Ma, Y Ren, J Xiong, B Guo, Y Song, S Liang and L Wu, *Appl. Catal. B-Environ.*, 2019, **243**, 10-18.

[12] Z Zhao, M M. F Espinosa, J Zhou, W Xue, X Duan, J Miao and Y Huang, *Nano Res.*, 2019, **12**, 1467-1472.

[13] J Li, M Li, H Sun, Z Ao, S Wang and S Liu, *ACS Catal.*, 2020, **10**, 3516-3525.

[14] P Zhu, Y Shen, L Dai, Q Yu, Z-M Zhang and C An, *ACS Appl. Mater. Inter.*, 2021, **14**, 1452-1459.

[15] Z Fang, P Zhang, M Wang, F Li, X Wu, K Fan and L Sun, *ACS Sustain. Chem. Eng.*, 2021, **9**, 11855-11861.

[16] J Wan, X Mu, Y Jin, J Zhu, Y Xiong and R Li, *Green Chem.*, 2022, **24**, 4870-4876.

[17] L Luo, Z-J Wang, X Xiang, D Yan and J Ye, *ACS Catal.*, 2020, **10**, 4906-4913.